Fault-Tolerant Control for Four-Wheels Independently Actuated Electric Vehicles

Farah Shalhoub[1], Majd Saied[1,2], Clovis Francis[3], Hussein Termous[4] and Hassan Shraim[1]

[1]*Scientific Research Center in Engineering, Faculty of Engineering, Lebanese University, Hadath, Lebanon*
farah.shalhoub@st.ul.edu.lb
majd.elsaied@ul.edu.lb
hassan.shraim@ul.edu.lb

[2]*Lebanese International University, Faculty of Engineering, Electrical and Electronics Engineering Department, Bekaa, Lebanon*

[3]*Arts et Metiers PariTech, Campus de Chalons en Champagne, Rue Saint Dominique 51000, Chalons en Champagne, France*
Clovis.francis@ensam.eu

[4]*Basic and Applied Sciences Research Center, Al Maaref University, Beirut, Lebanon*
hussein.termous@mu.edu.lb

ABSTRACT

This paper presents a novel Active Fault-Tolerant Control (AFTC) framework for a four-wheel drive (4WD) electric vehicle equipped with independently actuated in-wheel motors (IWMs). The presented approach consists of a fault detection and diagnosis (FDD) module and a compensation strategy. Once a fault is detected, the FDD module is activated, and as a consequence the fault will be identified, the faulty wheel will be isolated, and fault magnitude will be estimated. Then, based on the FDD module outputs, compensation module strategy is initiated. Compensation module employs a multi-parametric optimization technique to achieve the main objective of reducing the torque demand to the faulty actuator. Through extensive MATLAB/Simulink simulations, the results of this study showcase the effectiveness of the proposed AFTC system in managing multiplicative faults affecting the IWMs of the electric vehicle.

1. INTRODUCTION

Electric vehicles with four-wheel independent drive are considered a groundbreaking advancement in vehicle design, offering significant benefits due to their chassis architecture. These advantages include flexible actuation, rapid torque response, and the ability to control each wheel independently (Lian et al., 2025). As a result, extensive research efforts are being devoted to developing advanced stability control methods for this redundant system, with a particular focus on torque distribution strategies (Achdad et al., 2024), (Deng et al., 2023). In parallel with these developments, increasing demands on vehicle safety and passenger comfort have driven research toward the integration of advanced control frameworks that address the inherent complexity of fully autonomous vehicles. This has led to the emergence of Global Chassis Control (GCC), a control module designed to coordinate multiple actuators and achieve various control objectives simultaneously. Zhu et al. (2024) demonstrated a multilayer GCC integrating differential drive-assist steering with direct yaw control via a coordinated decision layer and a torque distribution layer, improving both handling and lateral stability. Similarly, the work in (Chokor et al., 2022) compares a centralized multi-layer LPV/H_∞ approach with a decentralized sliding-mode control scheme, highlighting different actuator coordination strategies based on stability metrics. More recent work continues this direction with integrated coordination frameworks that reconcile competing performance goals. For example, (Guo et al., 2024a) present a three-layer AMPC-based coordination architecture for distributed-drive EVs, and (Dong et al., 2023) optimize the coordinated AFS–DYC action for lateral stability.

While these technologies enhance driving flexibility and active safety, they also increase the likelihood of actuator faults due to the added system complexity and the higher number of actuators. This highlights the important role of

https://doi.org/10.36001/IJPHM.2026.v17i1.4622

fault-tolerant control (FTC) in maintaining and improving vehicle safety.

1.1. Related Works

A wide range of techniques have been employed in fault-tolerant control to ensure the stability of vehicles experiencing faults, including methods such as sliding mode control (Sun et al., 2024), (Lu & Xu, 2021) linear parameter-varying (LPV) control (Guo et al., 2024b), (Wang & Wang, 2018) and robust control (Sakthivel et al., 2020), (Guo & Chen, 2020). Passive FTC of these systems has attracted a lot of attention. Passive FTC is defined as the control approach that ensures system stability and acceptable performance in the presence of faults without requiring fault detection or system reconfiguration. The authors in (Chen et al., 2019) proposed a passive FTC scheme for an autonomous electric vehicle with in-wheel drives, treating actuator faults as uncertainties within a multiple-input multiple-output state-feedback framework to preserve path tracking and stability without explicit fault diagnosis or reconfiguration. Similarly, the work in (Tong et al., 2022) proposed an integrated vehicle control that consists of two main components: a Model Predictive Control (MPC) path-following module, which computes the required generalized forces/moments to track the reference trajectory and a passive FT layer based on sliding-mode control, which acts to preserve yaw stability and limit sideslip under in-wheel motor faults while mitigating chattering. While passive techniques are simpler and more robust than active techniques under certain conditions, they may fail to maintain stability or performance under faults that were not anticipated during the design phase. In addition, since faults are not explicitly detected or isolated, undetected faults may accumulate over time, potentially leading to progressive performance degradation or even system failure (Saied et al., 2020). Active Fault-Tolerant Control addresses this limitation by incorporating fault detection and diagnosis mechanisms, allowing the system to identify, isolate, and compensate for faults in real time. Following this perspective, the authors in (Wang et al., 2024) propose an approach that combines active FTC with a Reference Target Reshaping Scheme (RTRS) to address actuator faults in four-wheel independent drive vehicles. Based on the calculation of the Fault Tolerant Feasible Region, a control allocator for force distribution is designed. The development and integration of fault diagnosis modules essential for active fault-tolerant systems have received limited attention in existing research. The work in (Zhu et al., 2023) proposed an active motor fault-diagnosis scheme for distributed four-wheel independent-drive electric vehicles. Assuming a nominal path-tracking controller under healthy conditions, residuals are built from the ratio between expected and actual wheel-motor torque and then they are fed to a fuzzy logic classifier that outputs a per-wheel failure factor to detect and isolate the faulty in-wheel motor. The authors in (Zhu et al., 2025) proposed a data-driven fault diagnosis for such vehicles using a two-stream 2D-Convolutional Neural Network (CNN) that fuses time-domain signals with time–frequency maps, enhanced by a Depthwise Convolution Block Attention (DCBA) module. Tested across varying speeds/loads/roads, it achieves robust per-wheel fault detection and isolation without explicit vehicle modeling, outperforming single-stream baselines.

1.2. Motivation and Contribution

This work develops a unified active fault-tolerant control framework for a four-wheel independently actuated electric vehicle, aimed at tolerating actuator faults while preserving vehicle stability and trajectory tracking. Building on the general frameworks of (Laghmara et al., 2017) and (Tarhini, 2021), the proposed approach introduces two key advances:

- a behavior-based fault detection and isolation scheme that first identifies the faulty side of the vehicle and then applies a virtual gain-based estimation to isolate the individual faulty wheel and quantify its loss of effectiveness;
- the tight integration of this FDI scheme with a multi-parametric optimization-based torque allocator, which redistributes the driving torque among the four wheels according to the estimated degradation, while accounting for residual control capability, energy consumption, and safety constraints. This unified framework enables real-time diagnosis and compensation, extending beyond a simple combination of previously published techniques.

The main contributions of the paper are therefore summarized as follows:

- Proposition and validation of a behavior-based fault diagnosis scheme for actuator faults in a four-wheel independently actuated electric vehicle. The method combines side-level behavior analysis with virtual gain-based estimation to isolate the faulty wheel and estimate its loss of effectiveness.
- Development of an original torque allocation strategy within a multi-parametric optimization framework, which explicitly exploits the estimated loss of effectiveness to manage how torque is redistributed among the four wheels in the presence of a fault. The framework jointly considers residual control authority, energy efficiency, and safety constraints, thereby ensuring stable and safe vehicle operation under faulty conditions.

The structure of this paper is as follows: Section 2 outlines the implemented control strategy, detailing its hierarchical levels. In Section 3, the fault detection and isolation method is presented, along with the corresponding estimation approach. This section also evaluates the effectiveness and precision of the diagnostic process. Building on this

diagnosis, the fault compensation approach is developed in Section 4. Section 5 then showcases and analyses the outcomes achieved using the proposed active fault-tolerant control scheme, tested on a comprehensive vehicle model within a Matlab/Simulink environment. Finally, Section 7 concludes the paper and discusses potential directions for future research.

The vehicle models used in the following sections are mainly adopted from the works in (Termous et al., 2019) and (Chokor et al., 2016) and are built on Matlab/Simulink according to the parameters presented in Table 1. In this paper, the indices $i = \{f, r\}$ and $j = \{l, r\}$ denote the positions of the vehicle's wheels, representing front f, rear r and left l, right r sides respectively.

Symbol	Parameter	Value
M	Mass of the vehicle	$600\ Kg$
l_f	Distance from CG to the front axle	$\frac{2}{3}m$
l_r	Distance from CG to the rear axle	$\frac{4}{3}m$
t_f	Half front axle	$0.71\ m$
t_r	Half rear axle	$0.71\ m$
I_z	Yaw rate of inertia around CG	$360\ Kg.m^2$
r	Wheel effective radius	$0.3\ m$
h	Height from CG	$0.5\ m$
C_f	Front tire cornering stiffness	$34\ KN/rad$
C_r	Rear tire cornering stiffness	$19\ KN/rad$

Table 1. Model Vehicle Parameters

2. CONTROL ARCHITECTURE

Global Chassis Control (GCC) can be implemented using various architectural frameworks, including centralized, decentralized, and multi-layer structures. As demonstrated in (Chokor et al., 2022), each of these architectures offers unique advantages and challenges depending on the application and coordination needs. In this work, we adopt a multi-layer architecture inspired by the approach in (Tarhini, 2021). This structure, illustrated in Fig. 1, is organized into three distinct layers: the decision layer, the high-level control layer, and the low-level control layer. Each layer plays a specific role in managing vehicle dynamics and coordinating actuator behaviour effectively.

2.1. High-Level Control

2.1.1. Longitudinal Control

A Longitudinal control is crucial when it comes to providing stability and comfort to the driving experience. It aims at tracking the longitudinal velocity V_x to a desired velocity profile and thus regulates the vehicle's speed and acceleration and ensures safe and efficient motion in the direction of travel. The longitudinal velocity is produced by the full non-linear model of the vehicle and is obtained from the dynamics of the system according to Newton's laws. The control is

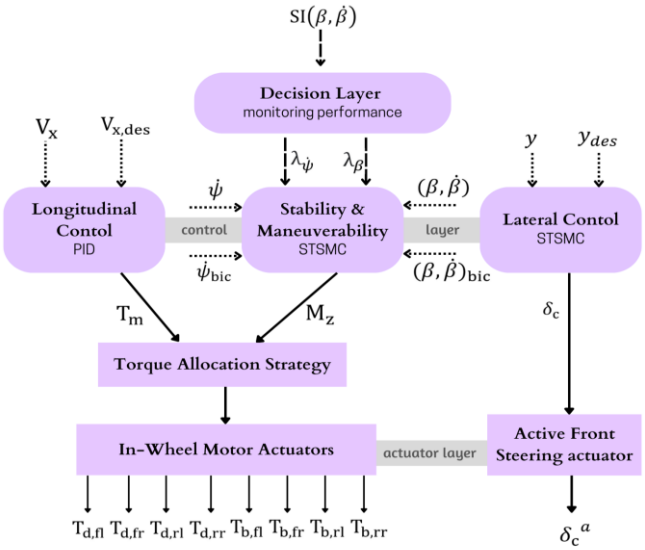

achieved in this work through a PID controller, represented by equation 1, that produces a total driving torque T_m as a control input into the system by driving the error $e_{v_x} = V_x - V_{x,des}$ to zero. The simple nature of the PID controller makes it a good choice to control the longitudinal behavior of the vehicle alongside the two more complex controllers used for the manoeuvrability and lateral control.

$$T_m = K_p e_{v_x} + K_i \int_0^t e_{v_x}\, d\tau + K_d \frac{d}{dt} e_{v_x} \qquad (1)$$

K_p, K_i, and K_d denote respectively the proportional, integral, and derivative gains of the controller carefully tuned to achieve the desired control performance. The control input generated from the longitudinal PID controller is the total driving torque T_m which will drive V_x to the desired profile after distributing the driving torques on the four independent in-wheel motors.

2.1.2. Stability and Maneuverability Control

These two control objectives will be achieved through the Direct Yaw-moment Control (DYC) controller on the same actuator; this requires careful coordination between the stability and manoeuvrability where the decision layer

prompts one objective over the other depending on the stability index of the vehicle and consequently generates decision variables λ_i to prompt the desired objectives based on a set of coordination rules, where $i = [\dot{\psi}, \dot{\beta}]$ with β denotes the side slip angle and ψ the yaw angle.
The sliding surfaces in defined in (Khelladi et al., 2020) are used here:

$$\begin{aligned} s_{\dot{\psi}} &= e_{\dot{\psi}} = \dot{\psi} - \dot{\psi}_{ref} \\ s_{\beta} &= \dot{e}_{\beta} + K_{\beta} e_{\beta} = \left(\dot{\beta} - \dot{\beta}_{ref}\right) + K_{\beta}(\beta - \beta_{ref}) \end{aligned} \tag{2}$$

$\dot{\psi}_{ref}$ and β_{ref} in equation 2 are modulated by the decision layer and its parameters $\lambda_{\dot{\psi}}$ and λ_{β} defined later in Section 2.2.

$$\begin{aligned} \dot{\psi}_{ref} &= \lambda_{\dot{\psi}} \dot{\psi}_{bic} + (1 - \lambda_{\dot{\psi}}) \dot{\psi} \\ \beta_{ref} &= \lambda_{\beta} \beta_{bic} + (1 - \lambda_{\beta}) \beta \end{aligned} \tag{3}$$

The surfaces $s_{\dot{\psi}}$ and s_{β} correspond to the control objectives for yaw rate and sideslip angle, respectively. However, to simultaneously regulate both variables through Direct Yaw Control (DYC), a new combined sliding surface is introduced:

$$s_{\dot{\psi},\beta} = c_1 s_{\psi} + c_2 s_{\beta} \tag{4}$$

Where c_1 and c_2 are positive constant weights, relatively scaling the sliding variables $s_{\dot{\psi}}$ and s_{β}, $s_{\dot{\psi},\beta}$ has a relative degree of 1 w.r.t the control input, hence:

$$\ddot{s}_{\dot{\psi},\beta}\left(s_{\dot{\psi},\beta}, t\right) = \Phi_{\psi,\beta}\left(s_{\dot{\psi},\beta}, t\right) + \xi_{\psi,\beta}(s_{\dot{\psi},\beta}, t)\, \dot{M}_z \tag{5}$$

Figure 1. Control architecture layers

The control input produced by this controller is the additive yaw moment M_z which guarantees the convergence of $s_{\dot{\psi},\beta}$ to zero in finite time and is presented below:

$$M_z = -\alpha_{M_{z,1}} \left|s_{\dot{\psi},\beta}\right|^{\tau_{M_z}} sign\left(s_{\dot{\psi},\beta}\right) - \alpha_{M_{z,2}} \int_0^t sign\left(s_{\dot{\psi},\beta}\right) d\tau \tag{6}$$

with τ_{M_z}, $\alpha_{M_{z,1}}$ and $\alpha_{M_{z,2}}$ being constants to be tuned.

2.1.3. Lateral Control

Trajectory following is an essential task for an autonomous electric vehicle. It is done by controlling the lateral dynamics of the vehicle. It is achieved in this work by reducing the lateral error between the vehicle's centre of gravity and the reference trajectory $e_y = Y_{CG} - Y_{CG,ref}$ to zero using the sliding mode control. Y_{CG} and $Y_{CG,ref}$ are determined using the equations of motion built into the validation and reference models respectively, as described in (Termous et al., 2019) and (Mtairek, 2020), and depicted in equation 7.

$$\begin{aligned} X_{CG}(t) &= \int (V_{x0} \cos\psi(\tau) - v_y(\tau) \sin\psi(\tau)) d\tau + X_{CG0} \\ Y_{CG}(t) &= \int (V_{x0} \sin\psi(\tau) + v_y(\tau) \cos\psi(\tau)) d\tau + Y_{CG0} \end{aligned} \tag{7}$$

The trajectory controller which is similarly explored in [24] is defined first by the sliding surface s_y.

$$s_y = \dot{e}_y + c_y e_y \tag{8}$$

It converges through the generated control input δ_c, defined in Equation 9, which represents the additional steering angle applied at the front wheels on top of the driver's original input.

$$\delta_c = -\alpha_{\delta,1} \left|s_y\right|^{\tau_{\delta}} sign\left(s_y\right) - \alpha_{\delta,2} \int_0^t sign\left(s_y\right) d\tau \tag{9}$$

The tuning parameters τ_{δ}, $\alpha_{\delta,1}$ and $\alpha_{\delta,2}$ are chosen such that they adhere to the constraints of the super-twisting algorithm. The tuned parameters of the controllers used throughout this study are summarized in Table 2.

Parameters	Value
K_p, K_i, K_d	$-35, -13, 0$
$\tau_{M_z}, \alpha_{M_{z,1}}, \alpha_{M_{z,2}}$	$0.5; 1300; 0.0001$
$\tau_{\delta}, \alpha_{\delta,1}, \alpha_{\delta,2}$	$0.5; 0.355; 0.0001$

Table 2. Controller's parameter for simulation

2.2. Decision Layer

Achieving effective global chassis control requires a well-orchestrated coordination among the three controllers described earlier. This coordination module is responsible for managing controller switching and assigning priorities based on driving conditions. At the heart of this process lies the real-time computation of the Stability Index (SI), which is derived from the vehicle's sideslip angle β and its rate of change $\dot{\beta}$. The SI, as defined in Equation 10 and originally introduced in (Doumiati et al., 2013), serves as a critical indicator of vehicle stability. According to the stability boundaries established in (He et al., 2006), the system is considered stable when $SI \leq 1$.

$$SI = |2.49\beta + 9.55\dot{\beta}| \tag{10}$$

Within the manoeuvrability and stability control unit, a coordinated strategy is implemented to strike a balance between two key objectives: achieving responsive manoeuvrability, represented by the yaw rate, and maintaining vehicle stability, indicated by the sideslip angle. For normal driving situations with no risk of instability, $SI \leq \underline{SI}$ the manoeuvrability control is always active ($\lambda_{\dot{\psi}} = 1$),

and the stability control is off $(\lambda_\beta = 0)$. However, if the vehicle is under a critical situation $SI \geq \overline{SI}$ the stability objective is prompted forth off $(\lambda_\beta = 1)$ while the manoeuvrability is turned off $(\lambda_{\dot{\psi}} = 0)$. The two decision variables $\lambda_{\dot{\psi}}$ and $\lambda_\beta \in [0,1]$ act as weighting factors inside the controller. They are modelled as sigmoid functions, given by Equation 11 to ensure a smooth transition:

$$\lambda_\beta = \frac{1}{1 + e^{-\frac{8}{\overline{SI} - \underline{SI}}\left(SI - \frac{\overline{SI} + \underline{SI}}{2}\right)}} \qquad (11)$$
$$\lambda_{\dot{\psi}} = 1 - \lambda_\beta$$

Previous studies have explored coordination strategies between active steering and differential braking. For example, (Bardawil et al., 2014) introduced several approaches that rely on the vehicle's stability index (SI), while (Termous et al., 2019) extended the coordination framework to include active suspension, aiming to enhance stability in critical driving scenarios. Although the Direct Yaw-Moment Control (DYC) and Active Front Steering (AFS) systems have each proven effective when applied independently, addressing stability and trajectory tracking respectively, their simultaneous application revealed conflicts that could compromise overall performance. To resolve this, a coordination strategy guided by the stability index is proposed to harmonize their actions and ensure the vehicle meets both manoeuvrability and stability goals.
The DYC being a limit handling stability controller, it should not affect the vehicle handling under normal driving conditions (Selby et al., 2001), thus it will only be promoted for $SI \geq \overline{SI}$ (critical driving). While the AFS will be active for normal driving situations. To emphasize the importance of the stability though, a weighting factor was included to give it more priority and to avoid interference between the two controllers which were observed to happen while testing the model. The tuning of the weighting factor is based on the system's behaviour observation.

2.3. Low-Level Control

Once the control inputs are determined at the decision level, they are passed down to the low-level controller, where they are translated into actionable commands for the vehicle's actuators. Before reaching the actuators, however, these inputs are processed by a torque allocation module. This critical step ensures that driving and braking torques are intelligently distributed among the four wheels, generating the necessary traction force (T_m) and yaw moment (M_z) to fulfill both longitudinal motion and stability or manoeuvrability objectives.

2.3.1. Torque Allocation

Torque vectoring, also known as torque allocation, refers to the strategy used to distribute the driving torques, originating from longitudinal control, and braking torques, generated by the Direct Yaw Control (DYC), across the wheels on the front and rear axles. This distribution plays a crucial role in optimizing vehicle performance, particularly in terms of stability and responsiveness. The specific method adopted in this work follows the approach detailed comprehensively in (Tarhini, 2021).
The core idea behind this approach is to allocate the total driving torque T_m, generated by the longitudinal controller, and the corrective yaw moment M_z, provided by the DYC controller, to each wheel in a way that aligns with the system's dynamic requirements. Thanks to the independence of each in-wheel motor, the system can create M_z by applying braking torque on one side of the vehicle while simultaneously delivering driving torque on the opposite side. This enables fully independent torque control across the wheels, significantly enhancing the controller's effectiveness. The distribution of both T_m and moment M_z is governed by four allocation parameters p, k, q, and n each ranging within $[0, 1]$.

To maintain pure longitudinal motion without inducing lateral drift, the total driving torque T_m is evenly split between the two wheels on each axle. This principle is reflected in Equation 12, which allocates T_m between the front and rear axles using a weighting factor p for the front axle and $(1 - p)$ for the rear axle:

$$\begin{cases} T_{rl} = T_{rr} = \frac{T_m}{2}(1 - p) \\ T_{fl} = T_{fr} = \frac{T_m}{2}(p) \end{cases} \qquad (12)$$

Since M_z is a free vector in space, its generation can be distributed between the front and rear axles to fully leverage the capabilities of the four independent in-wheel motors, as described in (Bardawil et al., 2014). This distribution is represented by the total torque contributions from the rear T_r and front T_f axles, as defined in Equation 13. A weighting parameter k controls how M_z is split, assigning a portion k to the rear and $(1 - k)$ to the front. The value of k effectively determines how much each axle contributes to producing the corrective yaw moment.

$$\begin{cases} T_r = -\frac{r}{t_r} k M_z \\ T_f = -\frac{r}{t_r}(1 - K) M_z \end{cases} \qquad (13)$$

where r is the wheel radius and t_r is the half rear axle distance. Once the total torques are allocated to the front and rear axles, they are further distributed to the individual wheels in a way that enables effective generation of the yaw moment M_z . This is achieved by applying opposite torques

on wheels of the same axle, braking on one side and accelerating on the other, ensuring that wheels on the same side (left or right) receive torques in the same direction. This torque symmetry respects a key constraint on yaw moment generation, helping to prevent over-acceleration or excessive braking, as highlighted in (Bardawil et al., 2014). The distribution is guided by parameters q and n, which control how T_r and T_f are split between the left and right wheels. A higher q increases braking on the rear wheels, while a lower value favours rear acceleration. Similarly, n adjusts the balance on the front axle, higher values bias toward front braking, and lower values toward front acceleration.

The torque distribution strategy is influenced by the desired direction of the yaw moment M_z . When a clockwise moment is needed, the torques are allocated to the wheels based on the following equation:

$$\begin{cases} T_{b,rr} = qT_r \\ T_{b,fr} = nT_f \\ T_{d,rl} = (1-q)T_r \\ T_{d,fl} = (1-n)T_f \end{cases} \tag{14}$$

while a counter-clockwise direction will result in the following equation:

$$\begin{cases} T_{b,rl} = qT_r \\ T_{b,fl} = nT_f \\ T_{d,rr} = (1-q)T_r \\ T_{d,fr} = (1-n)T_f \end{cases} \tag{15}$$

Where $T_{b,ij}$ and $T_{d,ij}$ represent the braking and accelerating torques at the wheel $i\,j$ respectively.

By varying the parameters p, k, q and n, the performance of the vehicle changes. Therefore, finding their optimal values will ensure the vehicle's optimal behaviour, guaranteeing both stability and energy efficiency.

To optimize the vehicle's performance, the goal is to balance the longitudinal forces between the front and rear wheels based on their respective loads. Initially, this is achieved according to the dynamic load distribution which utilizes internal vehicle dynamics to make the ratio of the longitudinal forces proportional to the loads between the rear and front sides of the vehicle. During vehicle manoeuvres the weight distribution changes leading to dynamic load transfer between front and rear axles. This transfer affects the traction and performance of the vehicle. To allow for a balance of the loads on the front and rear wheels, the Load Distribution Ratio κ is defined below:

$$\kappa = \frac{F_{z_f}}{F_{z_r}} = \frac{F_{z_{fr}} + F_{z_{fl}}}{F_{z_{rr}} + F_{z_{rl}}} \tag{16}$$

where $F_{z_{ij}}$ are the loads acting on the wheels as defined in (Bakker & Pacejka, 1987):

$$\begin{aligned} F_{z_{fl}} &= M\left(\frac{l_r}{l_r+l_f}g - \frac{h}{l_r+l_f}a_x\right)\times\left(\frac{1}{2} - \frac{h}{2t_f g}a_y\right) \\ F_{z_{fr}} &= M\left(\frac{l_r}{l_r+l_f}g - \frac{h}{l_r+l_f}a_x\right)\times\left(\frac{1}{2} + \frac{h}{2t_f g}a_y\right) \\ F_{z_{rl}} &= M\left(\frac{l_f}{l_r+l_f}g + \frac{h}{l_r+l_f}a_x\right)\times\left(\frac{1}{2} - \frac{h}{2t_r g}a_y\right) \\ F_{z_{rr}} &= M\left(\frac{l_f}{l_r+l_f}g + \frac{h}{l_r+l_f}a_x\right)\times\left(\frac{1}{2} + \frac{h}{2t_r g}a_y\right) \end{aligned} \tag{17}$$

with M being the mass of the vehicle, l_f and l_r are the distance from the centre of gravity to the front and rear axles respectively. t_f and t_r are the half front and rear axles respectively. h is the height from the centre of gravity. a_x and a_y are the longitudinal and lateral accelerations and g denotes the acceleration due to gravity.

The concept behind using dynamic load transfer for torque allocation is to adapt the driving torques applied to the front and rear axles, denoted by T_m in response to changes in load distribution. To ensure the wheels deliver the desired total torque T_m , the individual torque values are distributed according to the load distribution factor, p:

$$\kappa = \frac{F_{x_f}}{F_{x_r}} = \frac{pT_m/t_f}{(1-p)T_m/t_r} \tag{18}$$

where $t_f = t_r$ are half the front and rear track of the vehicle. Similarly, the generation of M_z is split as well according to this criterion while the braking and acceleration torques are divided equally between the wheels to ultimately realize M_z. Hence, the four allocation parameters are given by:

$$\begin{aligned} p &= \frac{F_{z_f}}{F_{z_f} + F_{z_r}} = \frac{\kappa}{1+\kappa} \\ K &= 1 - p = \frac{1}{1+\kappa} \\ q &= n = \frac{1}{2} \end{aligned} \tag{19}$$

2.3.2. Actuator's Model

The model of the actuators should consider the dynamic response with respect to the input signals. For this purpose, a simple model of the AFS and the Electro-Mechanical-Braking-System (EMB) actuators is used, as mentioned in (Doumiati et al., 2013) and (Chokor et al., 2022).

The additive steering angle due to the lateral control is achieved by the active front steering actuator which is a steer-by-wire active steering system that generates an additive angle applied to the front wheel axle. It is modelled as a Low pass filter described by:

$$\dot{\delta}_c = 2\pi f_1(\delta^+ - \delta_c) \tag{20}$$

where $f_1 = 10\ Hz$ is the cut-off frequency. The AFS actuator generates the additive steering angle δ_c that must track the generated control input δ^+. The output of this actuator is limited between $[-5, 5]$.

The active differential braking is generated by the brake-by-wire Electro-Mechanical-Braking-System to provide M_z. It is modeled as a low-pass filter as well described by:

$$\dot{T}_{b_{rj}} = 2\pi f_2(\overline{T}_{b_{rj}} - T^*_{b_{rj}}) \tag{21}$$

Where $f_2 = 10\,Hz$ is the cut-off frequency. The EMB actuator generates $T^*_{b_{rj}}$ to track $\overline{T}_{b_{rj}}$ which is the output of the low-level controller. The output of the actuator is limited between $[0, 1200]\ N.m$.

In addition, the in-wheel motor actuator model is presented as well in equation 22, which is a simplified first-order electric motor model to relate the torque command generated at the low level as $T_{d,ij}$ at each wheel, and the effective motor torque generated by the electric motor T^*_{ij} (Wang & Wang, 2018).

$$T^*_{ij} = \frac{T_{m,ij}}{1 + \frac{L_m}{R_m}s} \tag{22}$$

L_m and R_m are the motor's internal inductance and resistance respectively. This first-order model acts as low low-pass filter with a time delay due to the response time needed to generate the electric current to be transformed into torque on the motor shaft.

3. FAULT DIAGNOSIS

In a complex system such as an electric vehicle, the risk of faults, particularly in actuators, is relatively high. These faults can significantly impact driving dynamics and compromise handling performance. Whether they originate from in-wheel motors or other actuators like the Active Front Steering system, their effect on vehicle behaviour is often detrimental. As such, early detection and accurate diagnosis are critical to prevent potentially dangerous situations. The following sections focus specifically on faults in in-wheel motors. First, criteria for detecting which side of the vehicle are affected are introduced. Then, an estimation module, based on the virtual control gain approach described in (Laghmara et al., 2017), is developed to identify and localize the faulty wheel.

3.1. Actuator Fault Model

Before discussing the diagnosis and estimation of the in-wheel motor actuator faults, the motor fault can be modelled by the following equation:

$$T_{m,ij} = \lambda T^*_{m,ij} + \Delta T_{m,ij} \tag{23}$$

where $T_{m,ij}$ is the actual output of the IWM, while $T^*_{m,ij}$ is the desired output, $\lambda \in [0, 1]$ is the loss of effectiveness coefficient, and $\Delta T_{m,ij}$ is the additive fault. It can be seen that the fault-free case is for $\lambda = 1$ and $\Delta T_{m,ij} = 0$. This research will deal with multiplicative (loss of effectiveness) faults only, so for what follows $\Delta T_{m,ij} = 0$ which makes the fault model as in equation 24.

$$T_{m,ij} = \lambda T^*_{m,ij} \tag{24}$$

Loss of effectiveness (LOE) faults affecting one side of the vehicle can result in an uneven distribution of torque, leading to imbalances in yaw moment and a tendency for the vehicle to steer more to one side. This torque asymmetry between the left and right wheels disrupts the lateral force balance, negatively impacting the vehicle's lateral dynamics and potentially compromising stability. To analyse the vehicle's behaviour under various fault conditions, LOE faults were individually introduced to each wheel, as modelled in Equation 24. These scenarios also serve to evaluate the robustness of the control strategy in maintaining stable and predictable vehicle performance.

The example below illustrates a test run of a single lane change manoeuvre, performed at an initial speed of $80\ km/h$. At 2 seconds into the manoeuvre, a 20% loss of effectiveness is introduced in the front-right in-wheel motor. The vehicle's behaviour in both the controlled and uncontrolled fault cases is then compared to that of the healthy (fault-free) vehicle.

Figure 2 highlights the effect of the fault on the uncontrolled vehicle, which exhibits significant oversteering behaviour. In contrast, the controlled vehicle is able to maintain a trajectory closely aligned with that of the healthy (fault-free) vehicle, showing only minor deviations. This demonstrates the effectiveness of the robust control architecture in minimizing the performance gap caused by the fault. Even with a loss of effectiveness as high as 80%, the controlled vehicle maintains a trajectory error of approximately $0.23\,m$, compared to a much larger error of around 1 m in the uncontrolled case. Figure 3 further illustrates how the vehicle's internal dynamics are influenced by the fault, comparing both the controlled and uncontrolled scenarios against the reference model.

3.2. Fault Detection and Estimation

The control scheme proposed in section 2 can guarantee the stability and performance of the vehicle for the faults injected into the system as seen in section 3.1 with a slight degree of error. It can be seen that the two wheels on the same side have the same effect on the vehicle's behaviour in terms of speed, yaw, and trajectory as proposed by the authors in (Laghmara et al., 2017).

Furthermore, the tests conducted in this study suggest that a fault on the left side leads to under-steering, while a fault on the right side causes over-steering. Based on this, an active fault diagnosis is proposed in this section to locate which side of the vehicle has a faulty wheel actuator. Thus, the side of the vehicle where the fault occurs can be located by comparing the trajectory error of the actual trajectory of the vehicle to that of the vehicle under normal (no fault) driving conditions and then by thresholding this error to initiate the detection process. If the trajectory error exceeds the threshold, a left-side fault is identified; if it falls below the negative threshold, a right-side fault is identified.

The proposed method yields to an average detection time of $0.408\ s$ after fault injection. This result was obtained after several tests for different manoeuvres (single lane change (SLC), straight driving) at different velocities with varying magnitudes of faults on the wheels actuator. On average, faults of lesser severity took more time to be detected by the system, the average detection time for 10% loss of effectiveness (LOE) faults was $0.642\ s$ while faults with more severity like a 50% LOE were detected much earlier by the system with an average detection time of $0.268\ s$. Within the overall average detection time of $0.408\ s$ the average lateral drift for a single lane change (SLC) driving was equal to $3.58 \times 10^{-5}\ m$. Another significant index to examine is the stability index SI, where across 26 simulations with different conditions it exhibited an average increase of 16.78%.

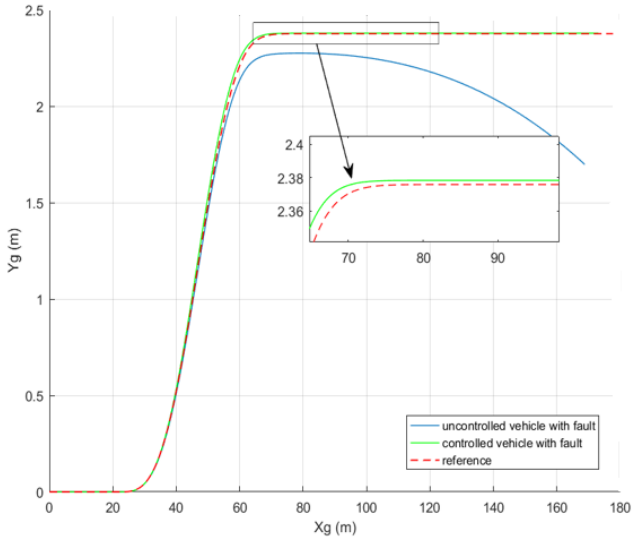

Figure 2. Trajectory of the vehicle with a 20% fault on front right IWM

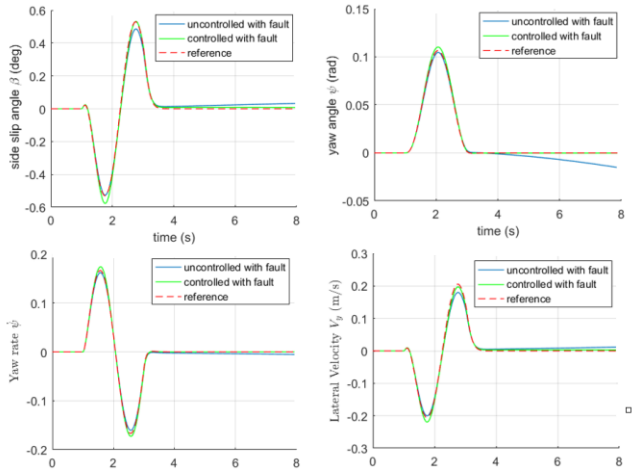

Figure 3. Inner dynamics of the vehicle in case of 20% fault on front right IWM

While a noticeable difference in vehicle behaviour allows detecting the faulty side of the vehicle, distinguishing the faulty in-wheel motor is hard since both wheels on the same side are driving wheels and thus manifest similar behaviour on the vehicle. The study conducted in (Laghmara et al., 2017) proposed in their work an active diagnosis method to introduce a virtual gain/fault into the system after the fault has been detected to isolate and estimate the fault. This method begins once the faulty side of the vehicle has been identified. At that point, the motor control gain can be virtually adjusted by scaling the control signal with a positive factor, denoted as α. This simulates an additional fault in the system but allows to estimate the magnitude of the loss of effectiveness coefficient.

For the healthy system and the faulty one, the following holds for two wheels on the faulty side j:

$$k_{f_j} T^*_{m_{fj}} + k_{r_j} T^*_{m_{rj}} = k_{0_{fj}} T^*_{m0_{fj}} + k_{0_{rj}} T^*_{m0_{rj}} \qquad (25)$$

Where $T^*_{m_{ij}}$ represents the torque on the front or rear wheel denoted by i on side j (left or right) under faulty conditions, while $T^*_{m0_{ij}}$ corresponds to the torque on the wheel i in the healthy scenario. The two unknown control parameters k_{fj} and k_{rj} represent the loss of effectiveness coefficient λ for the front and rear wheels for the faulty side j detected, and $k_{0_{fj}}$ and $k_{0_{rj}}$ for the ideal system equal to 1. To find the unknown parameters another equation is needed, and it is obtained after multiplying a virtual multiplicative fault of value α on either the front or rear wheel of the detected faulty side j. Thus, the new equation becomes:

$$\alpha k_{f_j} T^*_{m_{fj,n}} + k_{r_j} T^*_{m_{rj,n}} = k_{0_{fj}} T^*_{m0_{fj}} + k_{0_{rj}} T^*_{m0_{rj}} \qquad (26)$$

Consequently, the two parameters can be estimated for the suspected faulty side, where the parameter that deviates from 1 indicates the presence of a fault in the corresponding wheel. The two equations 25 and 26 are built into a fault estimation and isolation module in MATLAB. It processes torque inputs from both the faulty and non-faulty models along with the detected faulty side.

To better present the results of the estimation, the root-mean-square error (RMSE) is calculated for the different faults that were injected. RMSE measures the average difference between values predicted by a model and the actual values and is given by equation 27.

$$RMSE = \sqrt{\frac{\sum_{i=1}^{N}(x_i - \hat{x}_i)^2}{N}} \qquad (27)$$

where N is the number of data points, and x_i and $\hat{x}_i$ represent the actual observation and estimated value respectively.

Table 3 summarizes the RMSE values of the estimated loss of effectiveness coefficients that were tested on different wheels in different driving scenarios. For each LOE value 8 distinct experiments were done to obtain the RMSE values above. To evaluate the effectiveness of the estimation method, a tolerance range was chosen as stated to tolerate the estimation error of the fault and to obtain optimal results.

Error injected	Estimated ranges	RMSE
0.9	$0.897 - 0.93$	0.008
0.8	$0.86 - 0.8$	0.02
0.7	$0.72 - 0.64$	0.0389
0.6	$0.67 - 0.55$	0.041
0.5	$0.579 - 0.42$	0.047

Table 3. Estimated ranges of LOE coefficients and their mean RMSE

4. COMPENSATION

While the control architecture demonstrated strong fault tolerance, optimizing torque distribution to alleviate the load on the faulty motor remains essential for ensuring vehicle safety. In over-actuated systems, control reallocation strategies are particularly effective, allowing the redistribution of control efforts to healthy actuators, making them a key component in active fault-tolerant control frameworks. This section explores torque allocation through a multi-parametric optimization algorithm that adjusts four key parameters, (p, k, q, n), once a fault has been detected and estimated. The goal is to intelligently redistribute the control torque, easing the load on the faulty wheel while still preserving the vehicle's overall performance.

4.1. Cost Function

The objective of the multi-parametric optimization here is to reduce the torque on the faulty wheel by achieving an optimal distribution through the parameters p, k, q, and n that take into account the magnitude of the fault present on the wheel. The cost function proposed in (Tarhini, 2021), which was used for energy consumption optimization, includes terms related to the driving torques, rotational velocities, and the motor efficiency to build a power consumption model. The authors in (Tarhini, 2021) applied various optimization strategies, including the 2-step optimization with the cost function. They conducted an acceleration test and compared several performance indices, notably Accumulated Energy Consumption and Total Energy Gain. Their strategies showed promising results in terms of energy efficiency. In this work, we extended the use of this cost function and the 2-step optimization to consider the actuator fault on the wheel. For this reason, the cost function has been updated to include the loss of effectiveness coefficient estimated previously instead of the motor's efficiency, while the healthy motors will be given an efficiency of 1. In this way, the optimization will look to penalize the faulty motor and thus reducing the control effort on the faulty wheel.

Moreover, the distribution of the driving/braking torques is based on the direction of the yaw moment to be generated. Thus, two forms for the cost function are to be considered: the first one for the case where the required M_z is counter-clockwise, given by equation 28a, and the other one for the case where the required M_z is clock-wise, given by equation 28b. Then either of these functions is minimized accordingly.

$$\begin{aligned} f_1 = {} & \frac{T_m}{2}\left[(1-p)\left(\frac{\omega_{rl}}{\lambda_{rl}^{sign(T_m)}} + \frac{\omega_{rr}}{\lambda_{rr}^{sign(T_m)}}\right) + p\left(\frac{\omega_{fl}}{\lambda_{fl}^{sign(T_m)}} + \frac{\omega_{fr}}{\lambda_{fr}^{sign(T_m)}}\right)\right] \\ & + M_z\left(\frac{-r}{t_r}\right)\left[k\left[-q\,\frac{\omega_{rl}}{\lambda_{rl}^{sign(T_m)}} + (1-q)\frac{\omega_{rr}}{\lambda_{rr}^{sign(T_m)}}\right] + (1 \right. \\ & \left. - k)\left[-n\frac{\omega_{fr}}{\lambda_{fr}^{sign(T_m)}} + (1-n)\frac{\omega_{fl}}{\lambda_{fl}^{sign(T_m)}}\right]\right] \end{aligned} \qquad (28a)$$

$$f_1 = \frac{T_m}{2}\left[(1-p)\left(\frac{\omega_{rl}}{\lambda_{rl}^{sign(T_m)}}+\frac{\omega_{rr}}{\lambda_{rr}^{sign(T_m)}}\right) + p\left(\frac{\omega_{fl}}{\lambda_{fl}^{sign(T_m)}}+\frac{\omega_{fr}}{\lambda_{fr}^{sign(T_m)}}\right)\right] - M_z\left(\frac{-r}{t_r}\right)\left[k\left[-q\,\frac{\omega_{rr}}{\lambda_{rr}^{sign(T_m)}}+(1-q)\frac{\omega_{rl}}{\lambda_{rl}^{sign(T_m)}}\right]+(1-k)\left[-n\frac{\omega_{fl}}{\lambda_{fl}^{sign(T_m)}}+(1-n)\frac{\omega_{fr}}{\lambda_{fr}^{sign(T_m)}}\right]\right] \quad (28b)$$

4.2. Offline Optimization Problem: Two-Step Optimization Approach

Applying a two-step approach to this problem with four parameters that require optimization serves two purposes. Firstly, it reduces computational time, and more importantly, it enables us to achieve results that are more in line with proper vehicle behaviour. It works by pre-assigning q and n then obtaining p and k from the cost function.

Step 1: The first step will consist of assigning values for q and n according to the multi-objective criteria that considers the behaviour of the vehicle. This is done to relieve the vehicle from activating the braking through the DYC unnecessarily which causes wear for wheels if done for extended periods. Thus, by allowing q and n to be assigned according to the stability of the vehicle, DYC is only promoted when the vehicle is in critical driving conditions. The assignment works as follows:

- When the vehicle is in normal driving condition $SI \leq \underline{SI}$: the DYC is working for manoeuvrability objective meaning that M_z is generated solely by the traction torques. This gives $q = n = 0$ in the normal driving conditions which is the most common driving case.
- If the vehicle is experiencing a low stability error, then $\underline{SI} < SI \leq \overline{SI}$: in this scenario, the goal is to maintain the vehicle's longitudinal dynamics, ensuring it remains balanced while also conserving energy and avoiding abrupt acceleration or braking. In this context, generating M_z through half-driving/ half-braking actions is prioritized which gives $q = n = 0.5$.
- If $SI \geq \overline{SI}$: this indicates a critical driving situation where M_z needs to be generated by braking torques only, requiring $q = n = 1$.

Step 2: After obtaining q and n, they are used in the cost function as predetermined values then p and k are determined by minimizing the cost function. The objective here is to find a vector $x = [p\ k]^T$ that is a local minimum to the function $f(x)$ and is subject to constraints in equation 30, this makes up the objective function defined below:

$$\min_x f(x) \text{ subject to } \begin{cases} Ax \leq b \\ l_b \leq x \leq u_b \end{cases} \quad (29)$$

$$A = \begin{bmatrix} 1 & 0 \\ 0 & 1 \end{bmatrix} \quad b = \begin{bmatrix} 1 \\ 1 \end{bmatrix} \quad l_b = \begin{bmatrix} 0 \\ 0 \end{bmatrix} \quad u_b = \begin{bmatrix} 1 \\ 1 \end{bmatrix} \quad (30)$$

The problem is initialized with the vector x_0 in equation 31, setting each value to 0.5 as a midpoint between the defined constraint bounds.

$$x_0 = \begin{bmatrix} 0.5 \\ 0.5 \end{bmatrix} \quad (31)$$

The optimization is performed offline to reduce computational costs. In advance, optimized parameters are derived for various fault magnitudes and different faulty wheels. Subsequently, a lookup table is constructed to accommodate two fault magnitudes of 20%, 50% and two fault positions front and rear. The lookup table is designed to accept inputs, including estimates of the loss of the effectiveness coefficient and the location of the faulty wheel. It then interpolates to determine the appropriate p and k parameters for the vehicle, aligning with the objectives of torque reduction.

The lookup table, tailored for these two levels of LOE, provides a good range for the produced p and k parameters to effectively satisfy the objectives of better trajectory tracking, torque redistribution, and torque reduction on the faulty motor. Table 4 illustrates the impact of the p and k, produced by the look-up table, on the redistribution and subsequent compensation taking place on the motors of the vehicle

	Healthy Motor Torque		Faulty Motor Torque	
LOE Coefficient	Before	After	Before	After
0.9	9.18	22.466	23.08	7.863
0.8	9	21.348	23.9	7.439
0.7	10.22	25	24.76	6
0.6	11.05	27.9	25.57	4.5
0.5	11	29	26.36	3.2
0.4	13.985	29.54	27.179	4.03
0.3	14.412	30.03	28.03	4.102
0.2	14.902	30.5	28.99	4.172

Table 4. Torque redistribution before and after compensation using LUT

For certain induced loss of effectiveness values, the average torque on one of the healthy motors is presented before and after compensation as well as those of the faulty motor. It becomes evident that the redistribution effort works to increase the torque on the healthy motors and decrease it on the faulty one.

5. SIMULATION VALIDATION

A fault is injected onto the front left wheel at $t = 1.5s$ of 30% magnitude. The detection module detects the presence of fault at $1.809s$ and locates the faulty side. After the fault is detected, a virtual fault of magnitude $\alpha = 0.5$ is injected into the front left wheel; the estimation output is displayed in Fig. 4 below. The virtual fault injected after the fault detection, causes the estimation to rise for a few seconds as the system adjusts to the new fault injected as seen in Fig. 4 then it stabilizes to a true estimate of the fault.

The allocation parameters p and k seen in Fig. 5(a) and 5(b) are distributed as in section 2.3.1, where q and n are kept constant with 0.5.

After the fault occurs, the parameter p increases, indicating a shift in torque distribution toward the front wheels. This increase is later corrected by the robust control system, bringing it back in line with the healthy case. Similarly, parameter k decreases after the fault is injected, signifying increased yaw moment generation towards the front of the vehicle.

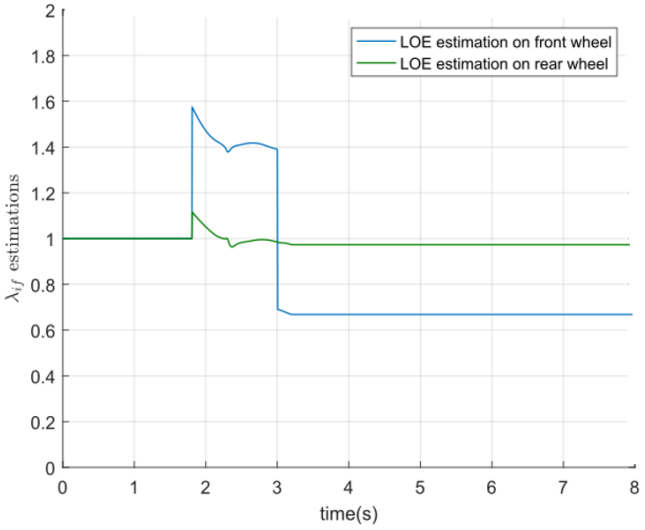

Figure 4. Estimation of the fault

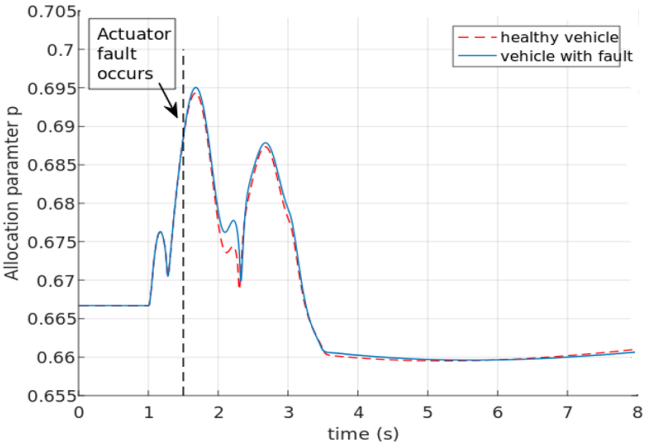

(a) Allocation parameter $\boldsymbol{p}$

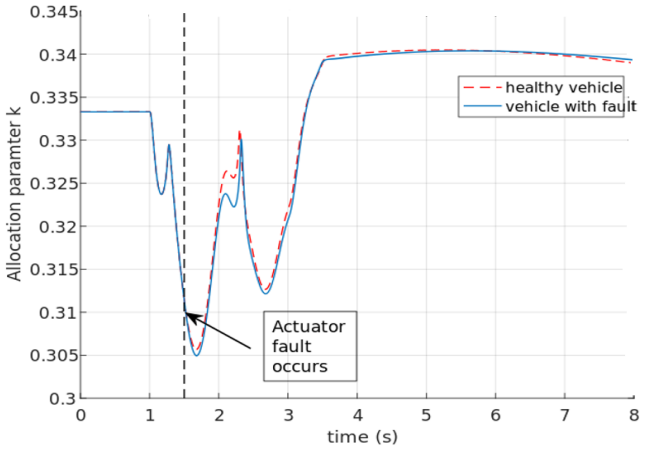

(b) Allocation parameter $\boldsymbol{k}$

Figure 5. Allocation parameters

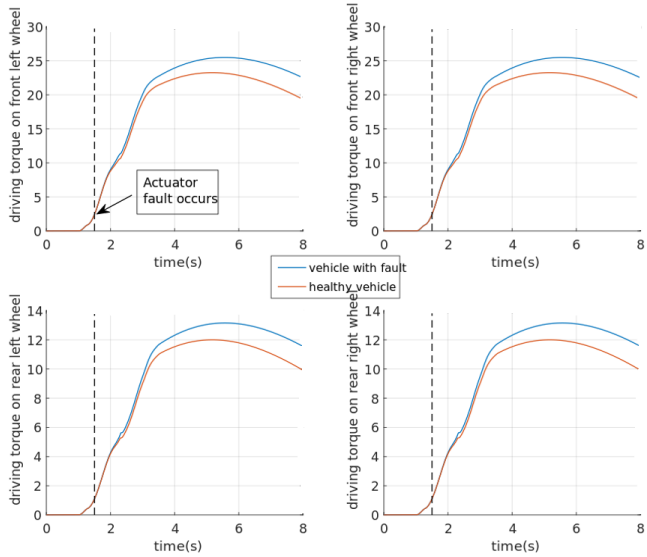

Figure 6. Driving torque demand to the IWM actuators

The torque demand to the IWM actuators increases after the fault occurs as a way for the robust controller to adjust in the presence of a fault, as shown in Fig. 6. As mentioned previously, increased torque demand to a faulty actuator can cause more harm and damage to the wheel, thus the compensation method proposed above is engaged after the isolation and estimation of the fault. The compensation is integrated into the model using a lookup table with predetermined values of p and k that are determined according to the location of the faulty wheel and the fault estimate. In this case, p and k are extrapolated from the lookup table and illustrated in Fig. 7(a) and 7(b) respectively and it is observed that the optimized parameters are engaged after the estimation around $t = 3.2s$ in this case. To elaborate on the figures, parameter p after compensation takes on values lower than the uncompensated assignment, which was previously around $p = 0.66$. This indicates that the production of driving torques is switched towards the rear wheels instead of the front wheels. Similarly, k was adjusted to take a higher value, indicating that the production of the corrective yaw moment shifts towards the rear wheels as well.

Moreover, the preassigned values for q and n according to 4.2 are zero in this SLC manoeuvre since the vehicle does not encounter instability, thus when the compensation is activated q and n shift from 0.5 to 0 meaning that the M_z is generated through acceleration on both sides.

As shown in Fig. 8, the compensated vehicle demonstrates improved trajectory tracking compared to the pre-compensation case. The zoomed-in view clearly shows that the optimized trajectory closely follows that of the healthy vehicle, with only minor fluctuations resulting from variations in the optimization parameters.

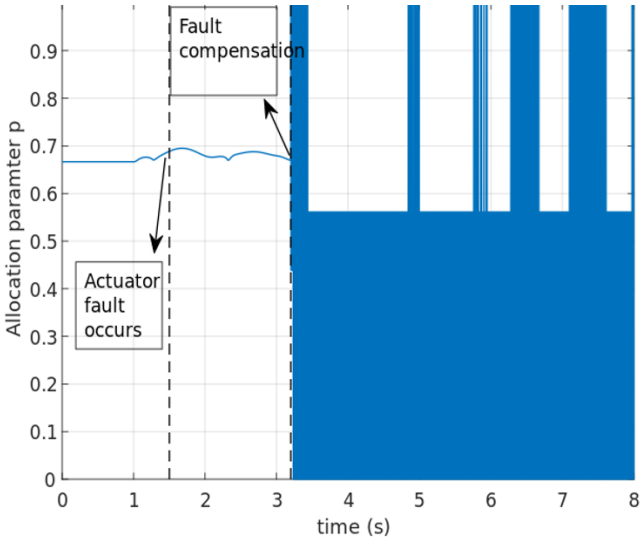

(a) Optimized parameter $\boldsymbol{p}$

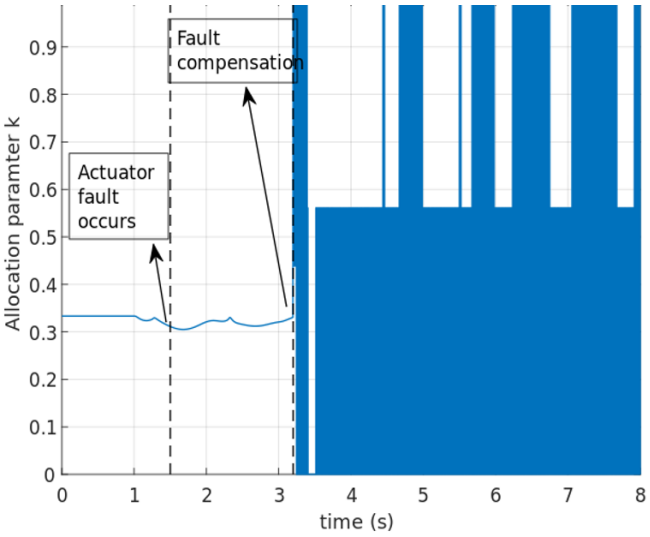

(b) Optimized parameter $\boldsymbol{k}$

Figure 7. Optimized parameters

The torques in Fig. 9 show that the torque demand on the front wheels is reduced while the demand on the rear wheels is increased significantly to make up for it. Consequently, the desired torque reduction on the faulty wheel and the re-distribution of torques to the other IWM is seen in effect in Fig. 10.

Although the input torques to the actuators experience oscillations that are related to those of the parameters p and k which are treated by the model of the actuator presented in equation 22. The actuator model filters out high oscillations and gives the output displayed in Fig. 10, which represents the torques generated by the wheels. The benefits of this

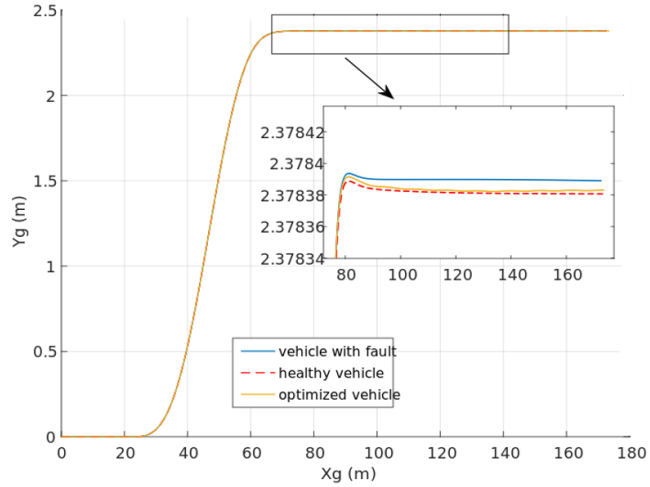

Figure 8. Trajectory of the vehicle after optimization

compensation strategy can also be observed in the inner dynamics of the system which are illustrated in the figures

below. Figure 11(*a*) shows that the compensation restored the yaw angle closely to the healthy vehicle although with some oscillations present. Also, in Fig. 11(*b*), the longitudinal velocity can be seen to have increased more than the healthy after the compensation started which is likely due to the absence of the braking torques allowing the vehicle to have more acceleration.

Overall, these results confirm that torque redistribution is essential for effective fault mitigation. While the robust controller alone responds to the fault by increasing torque demand, it is unable to reallocate this demand appropriately, leading to additional stress on the faulty actuator. In contrast, once the fault is detected and estimated, the proposed compensation strategy ensures proper torque redistribution across the healthy wheels, enhances overall stability, and restores vehicle performance close to healthy conditions.

6. CONCLUSION

This paper investigates the problem of active fault-tolerant control and compensation for four-wheel-drive electric vehicles. The study begins by implementing a robust control architecture to ensure vehicle stability and control under nominal and faulty conditions. Multiplicative faults affecting the in-wheel motor actuators were then modelled and individually simulated for each wheel to observe the specific impact on vehicle dynamics.

A fault diagnosis method was developed to identify the faulty side of the vehicle, left or right, based on behavioural indicators. Following detection, a virtual fault injection method was used to estimate the severity of the fault (i.e., the loss of effectiveness), enabling precise isolation of the faulty IWM. The final step involved fault compensation, achieved through an offline multi-parametric optimization strategy. This was integrated with a look-up table that redistributes torque in real time based on the detected and estimated fault conditions.

The key contribution of this work lies in its novel behaviour-based fault detection strategy, combined with a multi-parametric torque redistribution scheme tailored to the diagnosed fault. The offline-optimized look-up table proved effective across different fault magnitudes and can be enhanced further with additional system data to increase its adaptability.

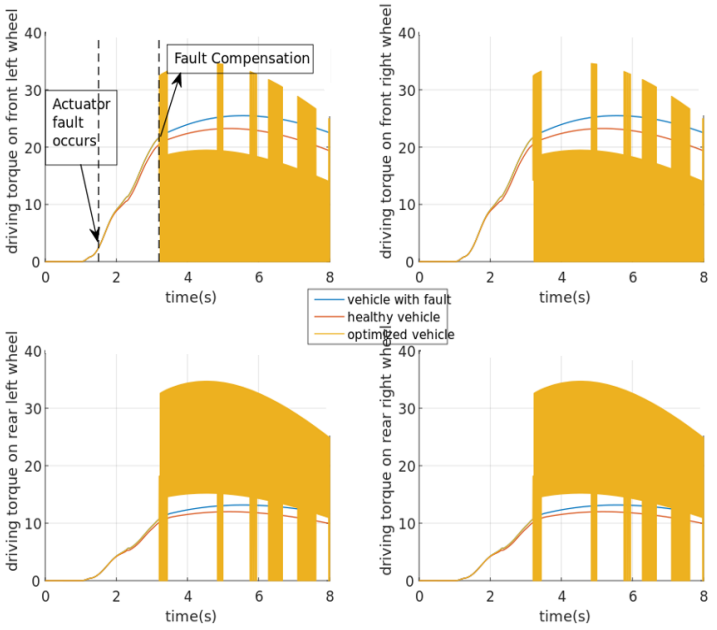

Figure 9. Driving torque demand to the IWM actuators, optimized

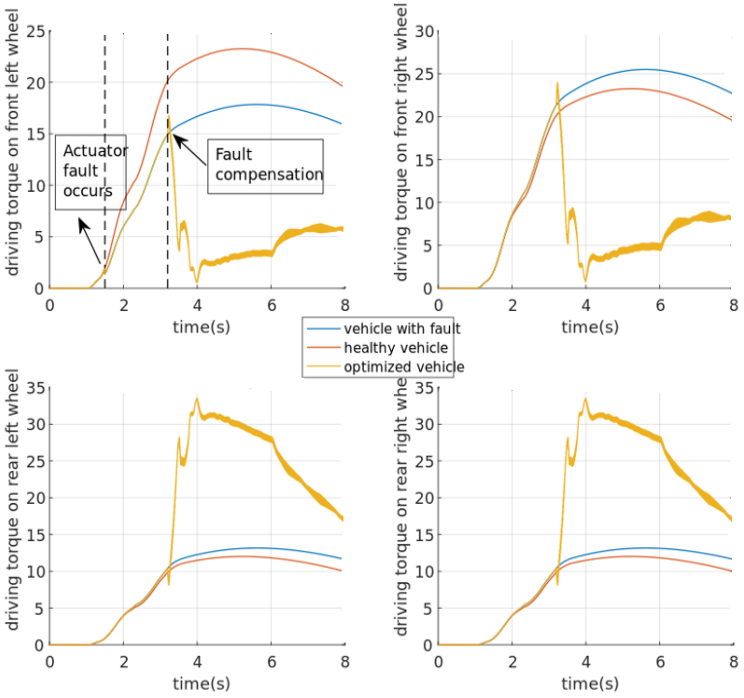

Figure 10. Driving Torques generated by the IWM, optimized

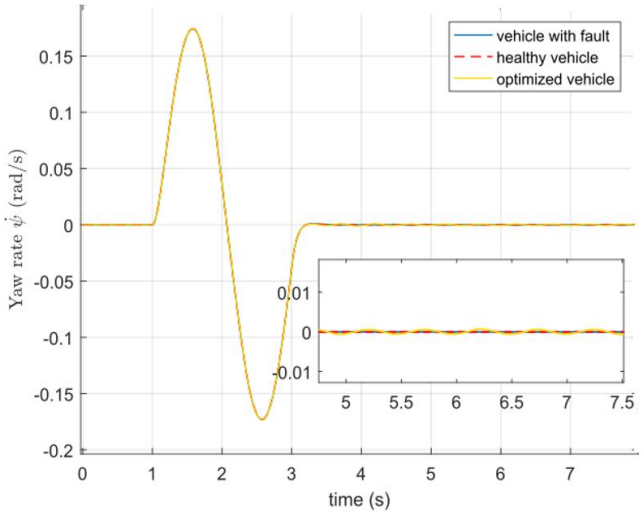

(a) Yaw rate

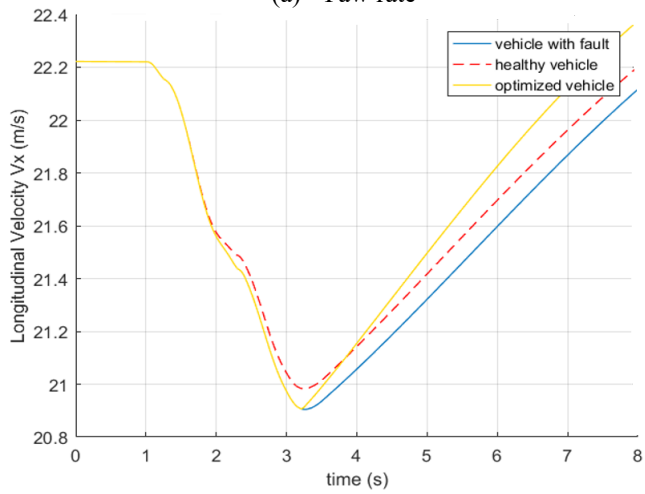

(b) Longitudinal Velocity

Figure 11. Yaw rate and Longitudinal velocity

Looking ahead, future work could extend the fault-tolerant framework to include additive faults in the IWMs, as well as faults in the active front steering actuator. Investigating the combined effects of multiple simultaneous faults and developing robust mitigation strategies would represent a significant and valuable direction for further research.

REFERENCES

Achdad, R., Rabhi, A. & Bosche, J. (2024). Energy-Efficient Torque Distribution Strategy for Four Wheel Drive Electric Vehicles Based on Traffic Zone. *IFAC-Papers Online,* 58(10), 1-6. doi: 10.1016/j.ifacol.2024.07.310.

Bardawil, C., Talj, R., Francis, C., Charara, A. & Doumiati, M. (2014). Integrated vehicle lateral stability control with different coordination strategies between active steering and differential braking. *17th International IEEE Conference on Intelligent Transportation Systems (ITSC)* (314-319), October 08-11, China. doi: 10.1109/ITSC.2014.6957710.

Chen, T., Chen, L., Xu, X., Cai, Y., Jiang, H. & Sun, X. (2019). Passive actuator-fault-tolerant path following control of autonomous ground electric vehicle with in-wheel motors. *Advances in Engineering Software*, 134, 22-30. doi.org/10.1016/j.advengsoft.2019.05.003.

Chokor, A., Talj, R., Charara, A., Shraim, H. & Francis, C. (2016). Active suspension control to improve passengers' comfort and vehicle's stability. *IEEE 19th International Conference on Intelligent Transportation Systems (ITSC)* (296–301), November 01-04, Brazil. doi: 10.1109/ITSC.*2016.7795570.*

Chokor, A., Talj, R. & Charara, A. (2022). A comparison between a centralised multilayer LPV/ $H\infty$ and a decentralised multilayer sliding mode control architectures for vehicle's global chassis control. *International Journal of Control*, 95(2), 303-318. doi: 10.1080/00207179.2020.1791360

Deng, H., Zhao, Y., Nguyen, A.T. & Huang, C. (2023). Fault-Tolerant Predictive Control with Deep-Reinforcement Learning Based Torque Distribution for Four In-Wheel Motor Drive Electric Vehicles. *IEEE/ASME Transactions on Mechatronics*, 28(2), 668-680. doi: 10.1109/TMECH.2022.3233705

Dong, J., Li, J., Gao, Q., Hu, J. & Liu, Z. (2024). Optimal coordinated control of active steering and direct yaw moment for distributed-driven electric vehicles. *Control Engineering Practice*, 134, 105486. doi: 10.1016/j.conengprac.2023.105486

Doumiati, M., Sename, O., Dugard, L., Martinez-Molina, J.-J., Gaspar, P. & Szabo, Z. (2013). Integrated vehicle dynamics control via coordination of active front steering and rear braking. *European Journal of Control*, 19(2), 121-143. doi: 10.1016/j.ejcon.2013.03.004

EgberBakker, L. N. and Pacejka, H. B., (1987). Tyre modelling for use in vehicle dynamics studies. *SAE Transactions*, 96, 190–204. doi: https://www.jstor.org/stable/44470677

Guo, B. & Chen, Y. (2020). Robust Adaptive Fault-Tolerant Control of Four-Wheel Independently Actuated Electric Vehicles. *IEEE Transactions on Industrial Informatics*, 16(5), 2882–2894. doi: 10.1109/TII.2018.2889292

Guo, J., Dai, Z., Liu, M., Xie, Z., Jiang, Y., Yang, H. & Xie, D. (2024a). Distributed Drive Electric Vehicle Handling Stability Coordination Control Framework Based on Adaptive Model Predictive Control. *Sensors*, 24(15), 4811. doi: 10.3390/s24154811

Guo, M., Bao, C., Cao, Q., Xu, F., Miao, X. & Wu, J. (2024b). Fault-Tolerant Control Study of Four-Wheel Independent Drive Electric Vehicles Based on Drive Actuator Faults. *Machines*, 12(7), 450. https://doi.org/10.3390/machines12070450

He, J., Crolla, D. A., Levesley, M. C. & Manning, W. J., (2006). Coordination of active steering, driveline, and braking for integrated vehicle dynamics control.

Proceedings of the Institution of Mechanical Engineers, Part D: Journal of Automobile Engineering, 220(10), 1401-1420. doi: 10.1243/09544070JAUTO

Khelladi, F., Orjuela, R. & Basset, M. (2020). Coordinated AFS and DYC for autonomous vehicle steerability and stability enhancement. *IFAC-PapersOnLine*, 53(2), 14248-14253. doi:10.1016/j.ifacol.2020.12.1160.

Laghmara, H., Doumiati, M., Talj, R. & Charara, A. (2017). Yaw moment Lyapunov based control for In-Wheel-Motor-Drive Electric Vehicle. *IFAC-PapersOnLine*, 50(1), 13828-13833. doi: 10.1016/j.ifacol.2017.08.2189

Lian, Y., Chen, G., & Liu, P. (2025). Study of Yaw Moment Control Strategy of Four-Wheel Independent Drive Electric vehicle. *Automotive Innovation*, 8, 157-168. doi: 10.1007/s42154-024-00287-y

Lu, M. & Xu, Z. (2021). Integrated Handling and Stability Control with AFS and DYC for 4WID–EVs via Dual Sliding Mode Control. *Aut. Control Comp. Sci.* 55, 243-252. doi.org/10.3103/S014641162103007X.

Mtairek, A., (2020). *Robust Vehicle Trajectory-Tracking Control*. Master Thesis, Lebanese University, Lebanon.

Saied, M., Lussier, B., Fantoni, I., Shraim, H. & Francis, C. (2020). Active versus passive fault-tolerant control of a redundant multirotor UAV. *The Aeronautical Journal*, 124 (1273), 385-408. doi: 10.1017/aer.2019.149

Sakthivel, R., Mohanapriya, S., Kaviarasan, B., Ren, Y. & Anthoni, S. M. (2020). Non-fragile control design and state estimation for vehicle dynamics subject to input delay and actuator faults. *IET Control Theory & Applications*, 14(1), 134-144. doi: 10.1049/iet-cta.2018.5967

Selby, M., Manning, W., Brown, M. & Crolla, D. (2001). A Coordination Approach for DYC and Active Front Steering. *SAE Transactions, Journal of Passenger car: Mechanical Systems Journal*, 110, 1411-1417. doi: https://www.jstor.org/stable/44730996

Sun, R., Wang, W., Yang, C., and Zhang, Y. (2024). Nonsingular Fast Terminal Sliding Mode Fault-Tolerant Control Scheme for Four-Wheel-Independent-Drive Electric Vehicles with Fault Observer. IFAC-PapersOnLine, 58(29), 58–63. doi: 10.1016/j.ifacol.2024.11.120

Tarhini, F., (2021). *Control architecture for an electric autonomous vehicle, equipped with 4 independent in-wheel electric motors*. Master Thesis, University of Technology of Compiegne, France.

Termous, H., Talj, R., Francis, C. Shraim, H. and Charara, A. (2019). Coordinated control strategies for active steering, differential braking and active suspension for vehicle stability, handling and safety improvement. *Vehicle System Dynamics*, 57(10), 1494-1529. doi: 10.1080/00423114.2018.1521001

Tong, Y., Li, C., Wang, G. & Jing, H. (2022). Integrated Path-Following and Fault-Tolerant Control for Four-Wheel Independent-Driving Electric Vehicles. *Automot. Innov.,* 5, 311-323. doi.org/10.1007/s42154-022-00187-z.

Wang, D., Gu, T. & Zhang, K. (2024). Fault Tolerant Control of 4-Wheel Independent Drive Vehicle Subject to Actuator Faults Based on Feasible Region. *IEEE Transactions on Vehicular Technology*, 73 (2), 1652-1666. doi: 10.1109/TVT.2023.3317010

Wang, R. & Wang, J. (2014). Actuator-Redundancy-Based Fault Diagnosis for Four-Wheel Independently Actuated Electric Vehicles. *IEEE Transactions on Intelligent Transportation Systems*, 15(1), 239-249. doi: 10.1109/TITS.2013.2277551

Wang, R. & Wang, J. (2018). Modeling and Fault-Tolerant-Control of Four-Wheel-Independent-Drive EVs. In: Zhang, H., Cao, D. & Du, H. Modeling, Dynamics and Control of Electrified Vehicles (409-449). Woodhead Publishing.

Zhu, J., Ouyang, X., Jiang, Z., Xu, Y., Xue, H., Yue, H. & Feng, H. (2025). In-Wheel Motor Fault Diagnosis Method Based on Two-Stream 2DCNNs with DCBA Module. *Sensors*, 25(15), 4617. doi.org/10.3390/s25154617

Zhu, S., Li, H., Wang, G., Kuang, C., Chen, H., Gao, G. & Xie, W. (2023). Research on Fault-Tolerant Control of Distributed-Drive Electric Vehicles Based on Fuzzy Fault Diagnosis. *Actuators*, 12(6), 246. doi.org/10.3390/act12060246

Zhu, S., Lu, J., Zhu, L., Chen, H., Gao, J. & Xie, W. (2024). Coordinated Control of Differential Drive-Assist Steering and Direct Yaw Moment Control for Distributed-Drive Electric Vehicles. *Electronics*, 13(18), 3711. doi: doi.org/10.3390/electronics13183711